EDGE ARTICLE

Check for updates

All publication charges for this article have been paid for by the Royal Society of Chemistry

Fe doping intensifies the built-in electric field for tailoring the reconstruction of sulfides towards efficient oxygen evolution†

Kun Wang, Chunmei Ni, Lei Jin, Xingyue Qian, Hui Xu, [iD] * Haiqun Chen [iD] * and Guangyu He*

The traditional view of sulfides as stable active centers has hindered the development of a clear structure–activity relationship and the rational design of high-performance oxygen evolution reaction (OER) catalysts. In this study, we focus on regulating sulfide reconstruction and have synthesized a Fe–Ni_3S_4/Cr_2O_3 pre-catalyst. Under the combined influence of the built-in electric field (BIEF) at the heterogeneous interface and Fe doping, both the sulfide reconstruction process and the electronic structure of the reconstructed product, namely Fe–NiOOH, were effectively tuned. The enhanced BIEF induced by Fe doping generated electron-rich regions on the sulfide surface, stabilizing the reconstruction process. Fe doping into the sulfide induced the incorporation of Fe into NiOOH, modulating the electronic states near the Fermi level of the metal–oxygen bond and subsequently activating the lattice oxygen mediated mechanism (LOM) of Fe–NiOOH, which serves as the true active center. Additionally, the BIEF optimized OH^- diffusion dynamics and the energy consumption of hydroxyl deprotonation, reducing the energy barrier of the rate-limiting step of the LOM process, further enhancing OER activity. Remarkably, Fe–Ni_3S_4/Cr_2O_3 demonstrated excellent OER activity and commercial viability. This work offers a new perspective on the regulation of reconstruction products of pre-catalyst, providing fresh insights for the design of efficient OER catalysts.

1. Introduction

The slow kinetics of the oxygen evolution reaction (OER) remain a critical challenge for the development of energy conversion and storage systems, such as water electrolysis for hydrogen production, regenerative fuel cells, and rechargeable metal–air batteries.[1,2] Consequently, the development of high-performance OER electrocatalysts to optimize reaction kinetics is essential.[3] Although non-precious metal sulfides offer advantages over commercial precious metal catalysts, such as abundant raw materials, low cost, and high structural stability, they still exhibit lower catalytic activity.[4,5] Based on the assumption that the catalytic reaction interface is stable during the OER process, with the metal active sites on the sulfide surface acting as the primary active centers, under the guidance of the adsorbate evolution mechanism (AEM), modification strategies such as defect engineering, heterostructure construction, and morphology regulation can optimize the

adsorption of oxygen-containing intermediates on metal sites ($OH^* \rightarrow O^* \rightarrow OOH^* \rightarrow O_2$), thereby enhancing the OER activity of sulfides.[6–8]

However, in recent years, with the ongoing advancement of research, it has been gradually revealed that sulfides used as electrocatalytic anode catalysts exhibit thermodynamic insta-bility at high anodic potentials, leading to structural evolution (reconstruction) during the OER process.[9] This has led to a shift in perspective, where sulfides are considered as "pre-catalysts", with the true catalytically active centers being the oxygen-containing species at higher metal oxidation states, such as metal oxyhydroxide (MOOH), amorphous metal-sulfur-oxide layers, and metal hydroxides, which are generated through surface reconstruction of the pre-catalysts.[10,11] Under the influ-ence of its unique high metal oxidation states and the interac-tions with the pre-catalyst, these oxygen-containing species typically exhibit excellent OER activity, resulting in catalytic performance that far exceeds that of the pre-catalyst.[4,12]

Thus, focusing solely on regulating the adsorption energies of oxygen-containing intermediates based on the traditional AEM overlooks the dynamic reconstruction behavior of sulfides during catalytic processes.[13,14] Furthermore, the constraints imposed by the scaling relationship of the AEM prevent the regulation of adsorption energies of different intermediates without mutual interference, which makes the 370 mV OER

Key Laboratory of Advanced Catalytic Materials and Technology, Advanced Catalysis and Green Manufacturing Collaborative Innovation Center Institution, Changzhou University, 21 Gehu Lake Road, Changzhou, 213164, China. E-mail: xuhui006@ cczu.edu.cn; chenhq@cczu.edu.cn; hegy@cczu.edu.cn

limiting overpotential predicted using AEM theory insufficient to explain the enhanced OER performance of sulfides reported in the literature.[15] Consequently, the traditional view of sulfides as stable active centers has impeded the development of a robust structure–activity relationship and the rational design of high-performance OER catalysts. Our research focuses on the regulation of the true catalytically active centers: the reconstruction products of sulfides. While much research has concentrated on understanding and characterizing the reconstruction process, there has been limited focus on controlling the reconstruction process and its products. The inherent properties of the pre-catalyst (including its electronic structure, chemical composition, crystallinity, and defects) and reaction conditions (such as applied voltage, pH, and electrolyte concentration) can all impact the reconstruction behavior.[11,16]

Based on this, by combining built-in electric field (BIEF) construction and doping strategies, we effectively tuned both the degree of reconstruction of the rationally designed pre-catalyst $Fe-Ni_3S_4/Cr_2O_3$ and the electronic structure of the true active site, Fe-doped nickel oxyhydroxide (Fe–NiOOH), formed during the reconstruction (Scheme 1). Due to the influence of the enhanced BIEF from Fe doping on the asymmetric charge distribution at the heterogeneous interface of $Fe-Ni_3S_4/Cr_2O_3$, the reconstruction of the electron-rich component $Fe-Ni_3S_4$ is stabilized, and the ion precipitation in the reaction process is reduced. Notably, the doping of Fe in the sulfide induces Fe atoms to be doped into the reconstructed product NiOOH, modulating the electronic states near the metal–oxygen bond Fermi level of Fe–NiOOH, thereby activating lattice oxygen and triggering the lattice oxygen mediated mechanism (LOM). This mechanism overcomes the limitations imposed by the scaling relationship of the traditional AEM. The $Fe-Ni_3S_4/Cr_2O_3$ catalyst exhibited an overpotential of 282 mV at a current density of 10 mA cm^{-2} in both 1 M KOH and simulated seawater electrolytes, and the assembled commercial electrochemical stack operated stably for 40 h. Moreover, the BIEF at the heterointerface further optimizes the diffusion kinetics of OH$^-$ and hydroxyl (OH*) deprotonation in the LOM process, further boosting OER activity. This work presents a new approach to the activity regulation of transition metal non-oxide materials, focusing on the active control of the reconstruction process and products.
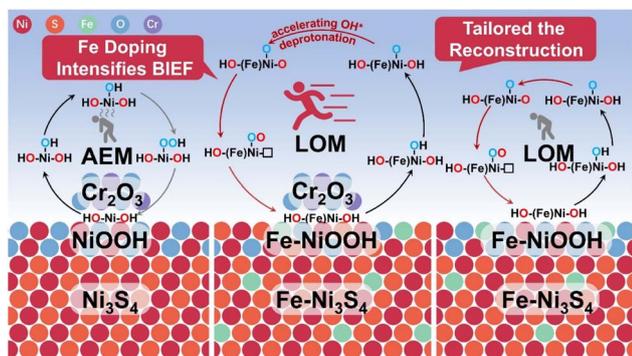
Scheme 1 Schematic diagram of the reconstruction degree and products regulated by the Fe doping-enhanced BIEF.

2. Materials and methods

Cr_2O_3 nanoparticles are obtained by calcining $Cr(OH)_3$ hydrate. Under magnetic stirring, 150 mL of 0.3 M NaOH is gradually added dropwise to 100 mL of 0.1 M $Cr(NO_3)_3 \cdot 9H_2O$ solution. The solid is then collected by centrifugation, followed by multiple washings with deionized water and ethanol. The resulting solid is dried to obtain $Cr(OH)_3$. Next, $Cr(OH)_3$ is calcined in air at 650 °C for 2 h with a heating rate of 2 °C min^{-1} to produce Cr_2O_3. Finally, the Cr_2O_3 and sulfide composite was prepared using a hydrothermal method.

In this step, 300 mg of the prepared Cr_2O_3 was dispersed in 40 mL of a solution containing 0.3 mmol of $FeSO_4 \cdot 7H_2O$, 2.7 mmol of $NiCl_2 \cdot 6H_2O$, 15 mmol of urea, 4 mmol $Na_2S_2O_3 \cdot 5H_2O$, 20 mL H_2O, and 20 mL ethylene glycol using ultrasonication. The dispersion was transferred to a 100 mL Teflon-lined stainless-steel autoclave and reacted at 180 °C for 15 h. After the reaction, the mixture was washed and filtered, and the obtained solid was vacuum-dried to yield the $Fe-Ni_3S_4/Cr_2O_3$ composite.

Using the same preparation method, $Fe-Ni_3S_4$ was synthesized without adding Cr_2O_3, Ni_3S_4/Cr_2O_3 was synthesized without adding $FeSO_4 \cdot 7H_2O$, and Ni_3S_4 was synthesized without adding Cr_2O_3 and $Fe(SO_4)_3 \cdot 7H_2O$. The aforementioned reagents were all procured from Sinopharm Group Reagent Co. Ltd, China.

3. Results and discussion

An $Fe-Ni_3S_4/Cr_2O_3$ pre-catalyst co-modified using Fe doping and the BIEF was prepared by a simple two-step method (Fig. 1a). First, $Cr(OH)_3$ was synthesized via a precipitation reaction between Cr salts and an alkali, followed by calcination to obtain Cr_2O_3 nanoparticles (Fig. S1†). Next, a solvothermal reaction was conducted using Fe salts, Ni salts, a sulfur source, and urea to prepare the $Fe-Ni_3S_4/Cr_2O_3$ heterojunction, with Cr_2O_3 nanoparticles encapsulated by $Fe-Ni_3S_4$. This unique encapsulated morphology was confirmed by TEM images (Fig. 1b and c). To investigate the effects of doping and the BIEF on the catalyst's structure and performance, the same method was used to prepare Ni_3S_4/Cr_2O_3 heterojunctions without Fe doping, as well as single-component Ni_3S_4 and $Fe-Ni_3S_4$ without Cr_2O_3. The crystal structures of $Fe-Ni_3S_4/Cr_2O_3$, Ni_3S_4/Cr_2O_3, and the single components were verified by X-ray diffraction (XRD) patterns shown in Fig. 1d. Notably, the enlarged XRD patterns reveal that, compared to single-component Ni_3S_4, the diffraction peaks of $Fe-Ni_3S_4/Cr_2O_3$, Ni_3S_4/Cr_2O_3, and $Fe-Ni_3S_4$ shifted to varying extents. This shift was attributed to Fe atom doping and the successful formation of the heterojunction, which rules out the possibility of a simple mechanical composite between $Fe-Ni_3S_4$ and Cr_2O_3 formed via the hydrothermal method (Fig. S2†). The crystal structure of $Fe-Ni_3S_4/Cr_2O_3$ was further confirmed by selected area electron diffraction (SAED), high-resolution TEM (HRTEM), and corresponding Fourier transform images (Fig. 1e and f). Scanning tunneling microscopy (STM) and elemental mapping revealed the uniform distribution of various elements in the $Fe-Ni_3S_4/Cr_2O_3$ composite (Fig. 1g).
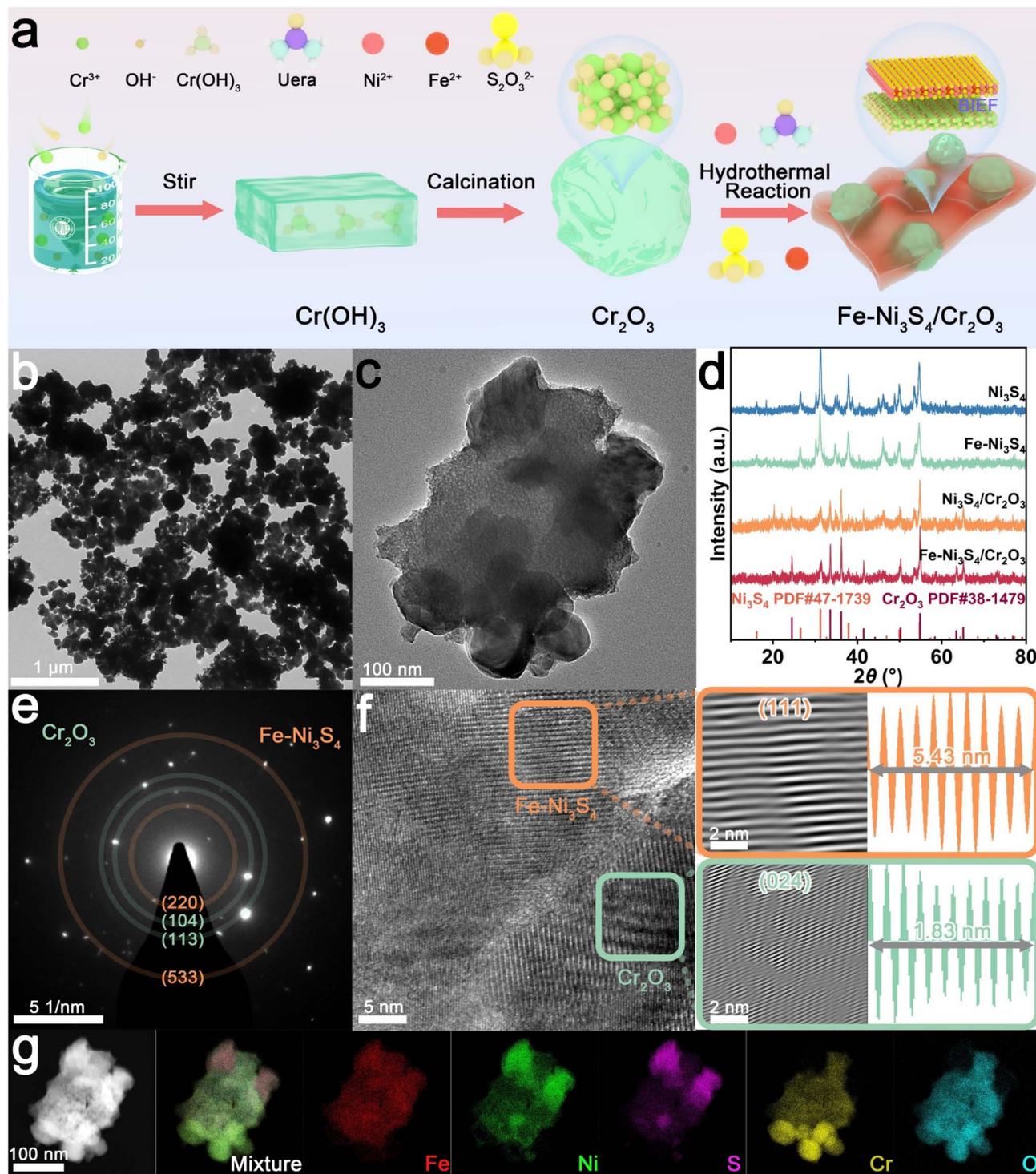
Fig. 1 (a) Schematic illustration of the synthesis of Fe−Ni$_3$S$_4$/Cr$_2$O$_3$. (b and c) TEM image of Fe−Ni$_3$S$_4$/Cr$_2$O$_3$. (d) XRD patterns of Ni$_3$S$_4$, Ni$_3$S$_4$/Cr$_2$O$_3$, Fe−Ni$_3$S$_4$, and Fe−Ni$_3$S$_4$/Cr$_2$O$_3$. (e) SAED pattern, (f) HRTEM image and corresponding Fourier transform images of Fe−Ni$_3$S$_4$/Cr$_2$O$_3$. (g) HAADF-STEM image and corresponding elemental mapping images of Fe−Ni$_3$S$_4$/Cr$_2$O$_3$.

Then we investigated the impact of heterojunction construction and Fe doping on the electronic structure of the pre-catalyst. In the Fe 2p X-ray photoelectron spectroscopy (XPS) spectrum of Fe−Ni$_3$S$_4$/Cr$_2$O$_3$ (Fig. 2a), the deconvolution peaks corresponding to Fe–S bonds, Fe^{3+}, and Fe^{2+} shifted to lower binding energies compared to those of Fe−Ni$_3$S$_4$. Similarly, in the Ni 2p XPS spectra of Fe−Ni$_3$S$_4$/Cr$_2$O$_3$ and Ni$_3$S$_4$/Cr$_2$O$_3$ (Fig. 2b), the deconvolution peaks for Ni^{3+} and Ni^{2+} also shifted to lower binding energies compared to those of Fe−Ni$_3$S$_4$, with those of Fe−Ni$_3$S$_4$/Cr$_2$O$_3$ exhibiting the greatest shift. A shift of
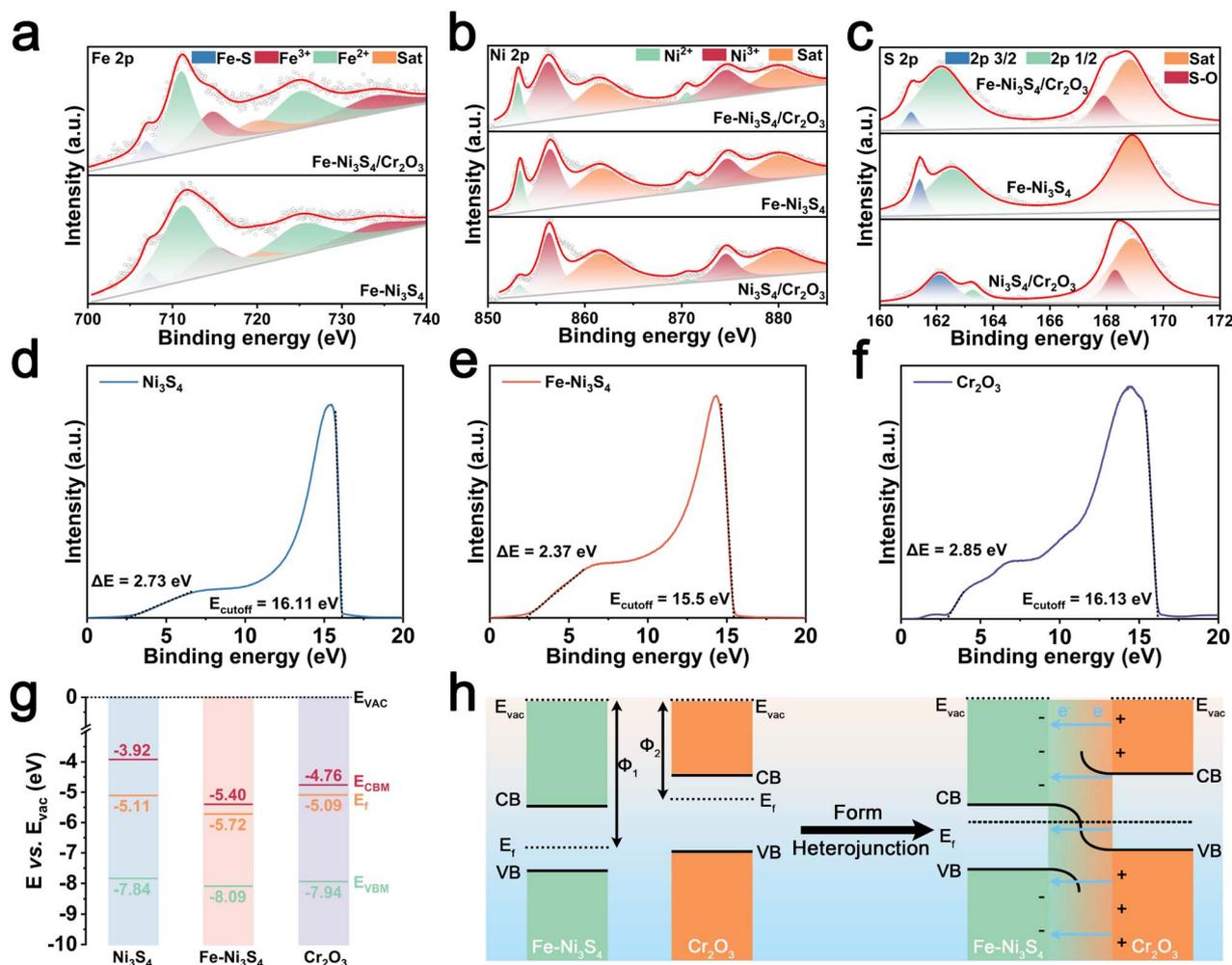
Fig. 2 High-resolution XPS patterns of (a) Fe 2p, (b) Ni 2p, and (c) S 2p. UPS spectra of (d) Ni_3S_4, (e) $Fe-Ni_3S_4$, and (f) Cr_2O_3. (g) Energy band diagram of Ni_3S_4, $Fe-Ni_3S_4$, and Cr_2O_3. (h) Schematic diagram of heterojunction formation of $Fe-Ni_3S_4/Cr_2O_3$.

XPS peaks to lower binding energies generally indicates a reduction in the binding energy of electrons on atomic orbitals, implying electron gains by the atoms. These shifts in the Fe 2p and Ni 2p XPS peaks suggest that the heterojunction construction induces electron enrichment in the sulfides of $Fe-Ni_3S_4/Cr_2O_3$. Furthermore, the S 2p XPS spectra of $Fe-Ni_3S_4/Cr_2O_3$, $Fe-Ni_3S_4$, and Ni_3S_4/Cr_2O_3 (Fig. 2c) show deviations in the deconvolution peaks for S $2p_{3/2}$ and S $2p_{1/2}$, indicating that doping and heterostructure construction affect the strength of the metal–sulfur bonds in the sulfides.

To further elucidate the electronic structure regulation, we characterized the energy band structure of the single component of the pre-catalyst. Mott–Schottky testing revealed that single component $Fe-Ni_3S_4$, Ni_3S_4, and Cr_2O_3 were all n-type semiconductors, and thus $Fe-Ni_3S_4/Cr_2O_3$ and Ni_3S_4/Cr_2O_3 are n–n junctions (Fig. S3†). Solid ultraviolet-visible (UV-vis) testing showed that the band gaps of $Fe-Ni_3S_4$, Ni_3S_4, and Cr_2O_3 are 2.69 eV, 3.92 eV, and 3.18 eV, respectively, suggesting that Fe doping reduces the band gap of the sulfides and enhances their conductivity (Fig. S4†). Subsequently, UPS measurements revealed that the work function (Φ) of $Fe-Ni_3S_4$, Ni_3S_4 and Cr_2O_3

is 5.72 eV, 5.11 eV and 5.09 eV, respectively, along with valence band parameters (Fig. 2d–f). Finally, the energy band structure diagram of the catalyst shown in Fig. 2g was obtained.

The difference in Φ between the sulfides and Cr_2O_3 drives the directional movement of electrons at the heterojunction interface until the Fermi levels of the two semiconductors are equalized, resulting in the spontaneous formation of a BIEF.[17–19] Since the Φ values of $Fe-Ni_3S_4$ and Ni_3S_4 are both lower than that of Cr_2O_3, the BIEF is directed from Cr_2O_3 to the sulfides, leading to charge transfer at the sulfide–Cr_2O_3 interface. This generates electron-rich regions on the sulfide surface and electron-deficient regions on the Cr_2O_3 surface, which explains the shift in the XPS deconvolution peaks of Fe and Ni in $Fe-Ni_3S_4/Cr_2O_3$ compared to those of $Fe-Ni_3S_4$. Moreover, Fe doping increases the Φ difference between the sulfides and Cr_2O_3, indicating a stronger BIEF in $Fe-Ni_3S_4/Cr_2O_3$ than that in Ni_3S_4/Cr_2O_3. Fe doping can effectively enhance the BIEF intensity between sulfides and Cr_2O_3, and the increase of the BIEF intensity will bring about more severe effects on the electron distribution at the heterogeneous interface (Fig. 2h).

The Fe doping enhanced BIEF effectively regulates the electronic structure of the sulfides. To assess the catalytic performance, we evaluated the electrochemical properties of the catalyst in a three-electrode system. First, we investigated the OER activity of the catalyst in a 1 M KOH electrolyte. The linear sweep voltammetry (LSV) results (Fig. 3a) and Tafel plots (Fig. 3b) demonstrate that Fe–Ni$_3$S$_4$/Cr$_2$O$_3$ exhibits optimal OER performance, showing an overpotential of only 282 mV at a current density of 10 mA cm^{-2} and a Tafel slope of 72 mV de^{-1}. Additionally, Fe–Ni$_3$S$_4$/Cr$_2$O$_3$ demonstrates a larger double-layer capacitance (C_{dl}) in the non-faradaic region, indicating a larger electrochemically active surface area (Fig. 3c and S5†). The Nyquist plot at 1.55 V shows that Fe–Ni$_3$S$_4$/Cr$_2$O$_3$ has the lowest charge transfer resistance (R_{ct}), further demonstrating its excellent reaction kinetics (Fig. 3d). It can be observed that the activity of Fe–Ni$_3$S$_4$/Cr$_2$O$_3$ is much higher than that of Fe–Ni$_3$S$_4$ and Cr$_2$O$_3$, and the activity of Ni$_3$S$_4$/Cr$_2$O$_3$ is much higher than that of Ni$_3$S$_4$ and Cr$_2$O$_3$, which have almost no OER activity (Fig. 3e). This indicates that the construction of the BIEF will significantly enhance the activity of sulfides and chromium oxide. Moreover, the activity of Fe–Ni$_3$S$_4$/Cr$_2$O$_3$ is

better than that of undoped Ni$_3$S$_4$/Cr$_2$O$_3$, showing the optimization of activity by Fe doping. When compared to similar reports in the literature, Fe–Ni$_3$S$_4$/Cr$_2$O$_3$ still demonstrates highly competitive OER activity (Fig. 3f and Table S1†). In stability tests, both multi-current chronopotentiometry (CP) (Fig. 3g) and a 100 h long-term stability test at a current density of 10 mA cm^{-2} (Fig. 3h) revealed that Fe–Ni$_3$S$_4$/Cr$_2$O$_3$ exhibited excellent reaction stability.

Given the scarcity of freshwater resources, we further evaluated the catalyst's performance in a simulated seawater electrolyte (Fig. S6 and S7†).[20,21] Fe–Ni$_3$S$_4$/Cr$_2$O$_3$ exhibited the same low overpotential of 282 mV and Tafel slope of 72 mV dec^{-1} at 10 mA cm^{-2} for OER in the simulated seawater electrolyte, significantly outperforming the referenced samples. Additionally, Fe–Ni$_3$S$_4$/Cr$_2$O$_3$ showed superior C_{dl} and R_{ct} values compared to the references. Notably, the OER activity of Fe–Ni$_3$S$_4$/Cr$_2$O$_3$ in simulated seawater was almost unaffected, while the activity of the comparison samples decreased significantly. To this end, we investigated the corrosion effect of Cl$^-$ on catalysts in simulated seawater mitigation through corrosion polarization curve tests. A higher corrosion potential (E_{corr}) and
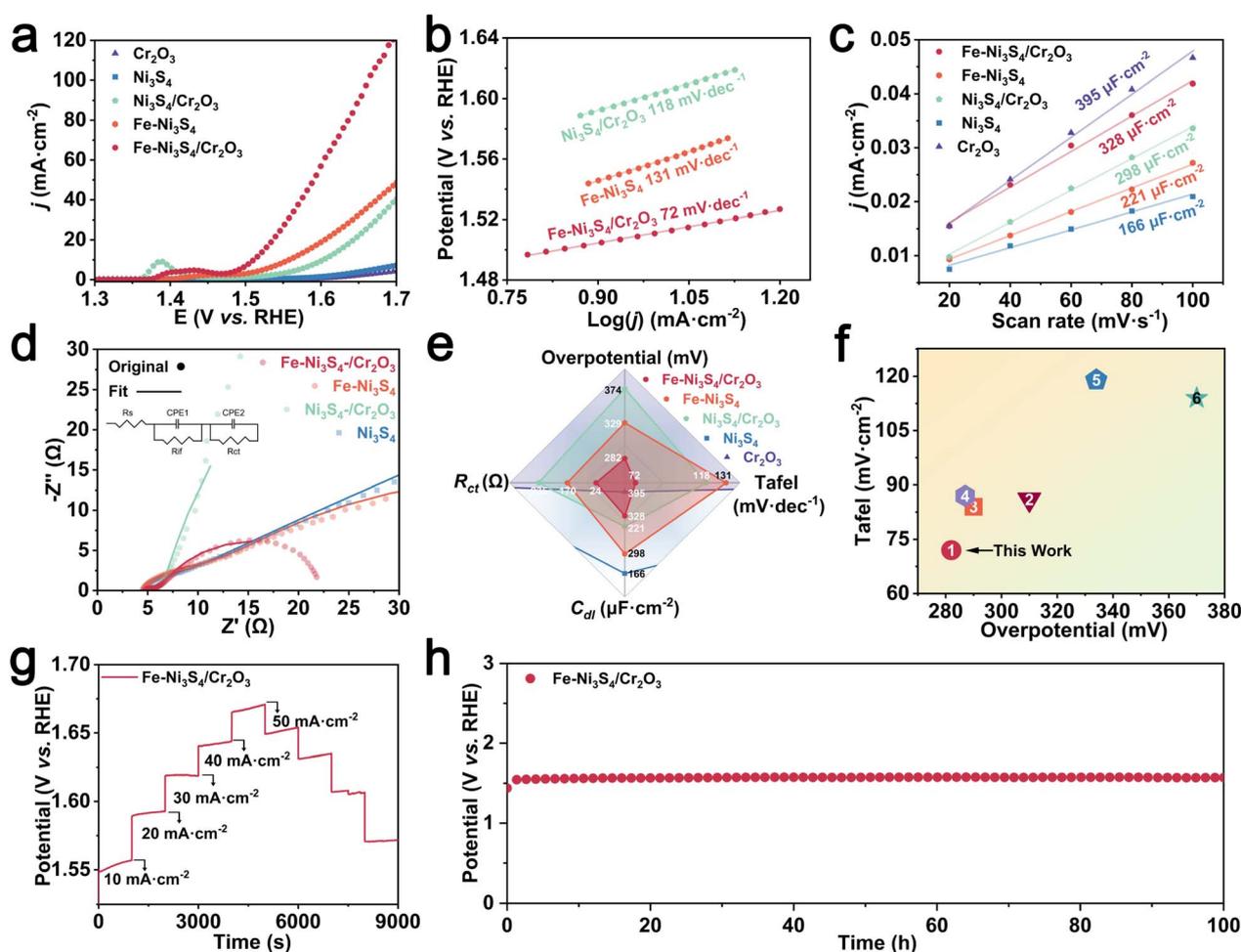

Fig. 3 OER activity in 1 M KOH solution. (a) LSV polarization curves, (b) Tafel plots, (c) C_{dl} values, and (d) Nyquist plots at 1.5 V *versus* RHE of Ni$_3$S$_4$, Ni$_3$S$_4$/Cr$_2$O$_3$, Fe–Ni$_3$S$_4$, and Fe–Ni$_3$S$_4$/Cr$_2$O$_3$. (e) Radar chart for comparison of comprehensive catalytic performance. (f) A comparison with other recently reported catalysts. (g) CP curve of Fe–Ni$_3$S$_4$/Cr$_2$O$_3$ at different current densities. (h) CP curve of Fe–Ni$_3$S$_4$/Cr$_2$O$_3$ at 10 mA cm^{-2}.

more negative corrosion current (I_{corr}) typically indicate better corrosion resistance. The results showed that, although the E_{corr} of Fe–Ni$_3$S$_4$/Cr$_2$O$_3$ was intermediate between those of Ni$_3$S$_4$, Fe–Ni$_3$S$_4$, Ni$_3$S$_4$/Cr$_2$O$_3$, and Cr$_2$O$_3$, its I_{corr} was the smallest, demonstrating its superior resistance to Cl$^-$ corrosion in seawater electrolysis. Fe–Ni$_3$S$_4$/Cr$_2$O$_3$ also exhibited excellent OER stability in simulated seawater, as evidenced by multi-current CP tests and 100 h CP tests. Finally, to evaluate the practical application potential of the catalyst, we used Fe–Ni$_3$S$_4$/Cr$_2$O$_3$ as the anode membrane electrode, commercial Pt/C as the cathode membrane electrode, and a proton exchange membrane as the separator to assemble a commercial-scale alkaline electrolyzer (AE) stack (Fig. S8a†). LSV testing and a 40 h stability test in 1 M KOH electrolyte confirmed the excellent commercial potential of the catalyst (Fig. S8b and c†).

To uncover the origin of the excellent catalytic activity of Fe–Ni$_3$S$_4$/Cr$_2$O$_3$, we investigated the influence of the Fe doping enhanced BIEF on the reconstruction behavior of the pre-catalyst and the formation of active sites during reconstruction. A 20 h chronoamperometry test at 1.6 V ensured sufficient reconstruction of the pre-catalyst (Fig. S9†). The reconstructed

pre-catalysts (denoted as Fe–Ni$_3$S$_4$/Cr$_2$O$_3$-A, Fe–Ni$_3$S$_4$-A, and Ni$_3$S$_4$/Cr$_2$O$_3$-A) were analyzed by XPS (Fig. 4a–d). Shifts in the binding energies of Fe, Ni, O, and S were observed, indicating the formation of new active species due to anodic reconstruction. Notably, the XPS spectra of S exhibited significant changes, with the disappearance of the S 2p$_{3/2}$ and S 2p$_{1/2}$ peaks after reconstruction, suggesting that no metal–sulfur bonds remained in the newly formed active species following sulfurization. Additionally, changes in metal oxidation states and oxygen-containing bonds were analyzed by fitting the relevant XPS peaks. As shown in Fig. 4g, after the chronoamperometry test, the proportion of high-valence metals and S–O electronic states significantly increased in Fe–Ni$_3$S$_4$/Cr$_2$O$_3$, Fe–Ni$_3$S$_4$, and Ni$_3$S$_4$/Cr$_2$O$_3$, indicating the formation of high-valence metal MOOH species and amorphous S–O metal species on the surface, signifying obvious reconstruction. In addition, we note that the proportion of high-valence metals and S–O electronic states in Fe–Ni$_3$S$_4$/Cr$_2$O$_3$-A is lower than those of Fe–Ni$_3$S$_4$-A and Ni$_3$S$_4$/Cr$_2$O$_3$-A. This is because the sulfide component of Fe–Ni$_3$S$_4$/Cr$_2$O$_3$ possesses more electrons than the sulfide in Ni$_3$S$_4$/Cr$_2$O$_3$ and single component Fe–Ni$_3$S$_4$ under the influence of
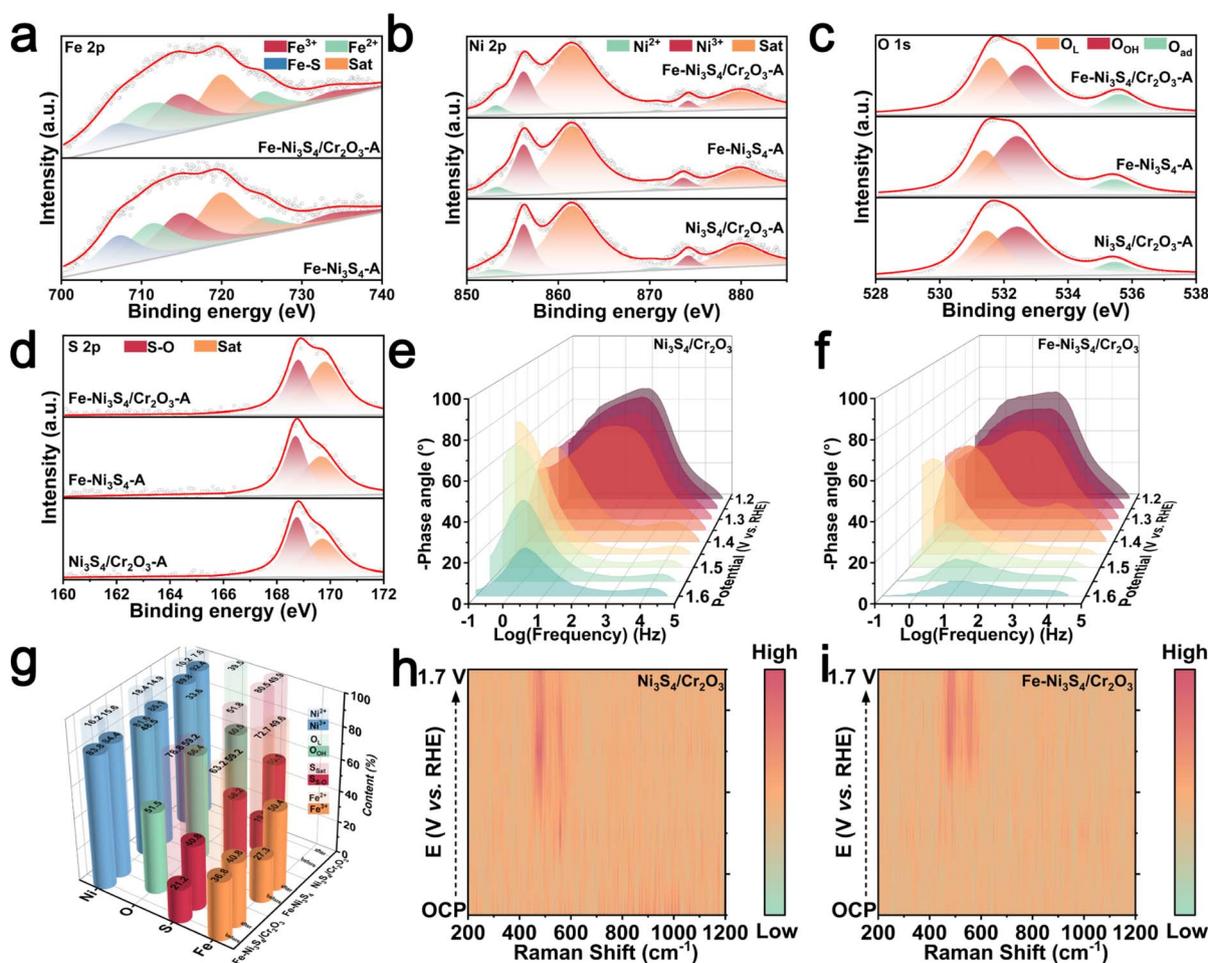

Fig. 4 High-resolution XPS patterns of the catalyst before and after stability testing. (a) Fe 2p (b) Ni 2p (c) O 1s, and (d) S 2p. Bode phase plots of *in situ* EIS on (e) Ni$_3$S$_4$/Cr$_2$O$_3$ and (f) Fe–Ni$_3$S$_4$/Cr$_2$O$_3$. (g) Histograms of the ratios of Ni^{2+}, Ni^{3+}, Fe^{2+}, Fe^{3+}, O$_L$, O$_{OH}$, S$_{sat}$, and S$_{S-O}$ in Ni$_3$S$_4$/Cr$_2$O$_3$, Fe–Ni$_3$S$_4$, and Fe–Ni$_3$S$_4$/Cr$_2$O$_3$ before and after reconstruction. *Operando* Raman spectra of (h) Ni$_3$S$_4$/Cr$_2$O$_3$ and (i) Fe–Ni$_3$S$_4$/Cr$_2$O$_3$.

the Fe doping enhanced BIEF. The electron-rich state of the sulfide from Fe–Ni_3S_4/Cr_2O_3 prevents the structural oxidation at high anode potential, which results in the inhibition of the reconstruction behavior in the OER.

This was further confirmed by inductively coupled plasma (ICP) analysis. As is well known, the reconstruction of sulfides, especially the formation of active MOOH species, is typically accompanied by the leaching of S ions. The amount of S leaching in the electrolyte after the OER is the lowest, which also indicates the inhibited reconstruction of sulfide in Fe–Ni_3S_4/Cr_2O_3 (Fig. S10†). In addition, the reduced Fe and Ni leaching from Fe–Ni_3S_4/Cr_2O_3 highlights the catalyst's improved structural stability during reconstruction. The suppressed reconstruction of sulfides in Fe–Ni_3S_4/Cr_2O_3 helps prevent conductivity loss and mitigate the weakening of synergistic effects between the true active sites and the pre-catalyst.

The Bode phase diagrams of Fe–Ni_3S_4/Cr_2O_3, Ni_3S_4/Cr_2O_3, and Fe–Ni_3S_4 all show a peak signal in the high frequency region, which indicates that the reconstruction occurs (Fig. 4e and f and S11†).[22,23] Additionally, the slightly lower reconstruction peak signal in Fe–Ni_3S_4/Cr_2O_3 further suggests that the Fe doping enhanced BIEF inhibits the reconstruction of the sulfide component. In situ Raman spectroscopy (Fig. 4h, i and S12†) also revealed the active species formed after reconstruction of the pre-catalyst. Characteristic peaks at 479 cm^{-1} and 558 cm^{-1}, corresponding to MOOH e_g bending and A_{1g} stretching vibrations, were observed in Fe–Ni_3S_4/Cr_2O_3, Fe–Ni_3S_4, and Ni_3S_4/Cr_2O_3, confirming that the reconstruction products were predominantly MOOH.[24,25] Based on the elemental composition of the pre-catalyst, we concluded that the reconstruction products of Fe–Ni_3S_4/Cr_2O_3 and Fe–Ni_3S_4 were Fe–NiOOH, while the reconstruction product of Ni_3S_4/Cr_2O_3 was NiOOH. The presence of Fe–NiOOH peaks within a narrow voltage range in Fe–Ni_3S_4/Cr_2O_3 further supports the conclusion that the enhanced BIEF suppresses the degree of reconstruction. In conclusion, the Fe-doping enhanced BIEF interferes with the reconstruction behavior of Fe–Ni_3S_4/Cr_2O_3, suppresses the excessive reconstruction of the sulfide component, and improves the catalyst's structural stability. Moreover, it successfully modifies the true active sites, leading to the formation of Fe-doped NiOOH active species on the catalyst surface, which enhances OER activity.

The reaction mechanism of the OER catalyst directly influences its catalytic activity. Therefore, we further explored the OER mechanism of Fe–NiOOH, which is the true catalytic center of Fe–Ni_3S_4/Cr_2O_3 restructures under the Fe-doped enhanced BIEF. We first evaluated the OER activity and pH dependence of the catalyst in KOH electrolytes with varying pH values (Fig. S13†). As shown in Fig. 5a, Fe–Ni_3S_4/Cr_2O_3 and Fe–Ni_3S_4 exhibited significant fluctuations in the reaction currents at the rated OER operating voltage, indicating strong pH dependence. This is because the O as the redox center in the LOM can tolerate a certain degree of charge accumulation in the reaction process, and the non-concerted proton-electron transfer decoupling in the process of OH* deprotonation makes the OH* deprotonation sensitive to the pH of the electrolyte, which leads to the dependence of the active pH of the OER.[26] The marked pH dependence of Fe–Ni_3S_4/Cr_2O_3 and Fe–Ni_3S_4

confirms that their true active center Fe–NiOOH triggers the LOM. In contrast, the conventional AEM, where metals act as the redox center and involve concerted electron and proton transfer during OH* deprotonation, shows negligible pH dependence in the catalyst's activity. Thus, the true active center NiOOH of Ni_3S_4/Cr_2O_3 and Ni_3S_4 follows the AEM.

TMAOH intermediate trapping experiments can further confirm the activation of the LOM in Fe–Ni_3S_4/Cr_2O_3 and Fe–Ni_3S_4, where Fe–NiOOH is the true active site. In LOM-based catalysts, oxygen from the catalyst lattice couples with surface-adsorbed oxygen to form a unique peroxo-like negative species (O_2^{2-}). The tetra-methylammonium cation (TMA^+) can trap O_2^{2-} via strong electrostatic interactions, inhibiting the further release of O_2.[27,28] As shown in Fig. 5b and S14,† the OER activity of Fe–Ni_3S_4/Cr_2O_3 and Fe–Ni_3S_4 was significantly suppressed upon TMAOH addition, while that of Ni_3S_4/Cr_2O_3 and Ni_3S_4 remained nearly unaffected. This also indicates the triggering of the LOM at the true active site Fe–NiOOH from Fe–Ni_3S_4/Cr_2O_3 and Fe–Ni_3S_4. Due to the influence of Fe doping on the electronic structure of the pre-catalyst and the reconstructed product, the triggered LOM of Fe–NiOOH (the true catalytic activity center after Fe–Ni_3S_4/Cr_2O_3 and Fe–Ni_3S_4 reconstruction) avoids the formation of high binding energy OOH* from the AEM of NiOOH (the true catalytic activity center of Ni_3S_4/Cr_2O_3 and Ni_3S_4 after reconstruction), thereby breaking the limitation of the scaling relationship and significantly enhancing the OER activity.

Based on electrochemical performance testing results, we found that although both Fe–Ni_3S_4/Cr_2O_3 and Fe–Ni_3S_4 activate the LOM, the OER activity of Fe–Ni_3S_4/Cr_2O_3 far exceeds that of single-component Fe–Ni_3S_4. Research indicates that the OER mechanism switches from the AEM to the LOM, where the electron transfer in the OH* deprotonation process changes from delocalized metal orbitals to higher energy localized oxygen non-bonding states. As a result, OH* deprotonation becomes the rate-determining step of the LOM, thereby influencing OER activity. To reveal the impact of the BIEF on the reaction mechanism, we conducted methanol molecular probe experiments.

The nucleophilic reagent methanol can capture the electrophilic species OH*, creating strong competition for OH* adsorption between the methanol oxidation reaction and the OER. Therefore, methanol, used as a probe, can detect the adsorption ability of OH*.[29] Fig. 5c shows that the current density of Fe–Ni_3S_4/Cr_2O_3 changed less than that of Fe–Ni_3S_4 after adding methanol, indicating that Fe–Ni_3S_4/Cr_2O_3 has a lower OH* adsorption energy. This is attributed to the BIEF at the heterogeneous interface of Fe–Ni_3S_4/Cr_2O_3, which also regulates the electronic structure of FeOOH. The reduced adsorption energy of OH* thermodynamically favors the subsequent OH* deprotonation, thereby accelerating LOM.

Additionally, we also studied the effect of the Fe doping-enhanced BIEF on the catalyst's surface microenvironment. The minimal differential capacitance of the dilute electrolyte can determine the catalyst's potential of zero charge (PZC), which is defined as the potential at which no excess charge exists on the electrode surface (Fig. 5d, e and S15†).[30] PZC is
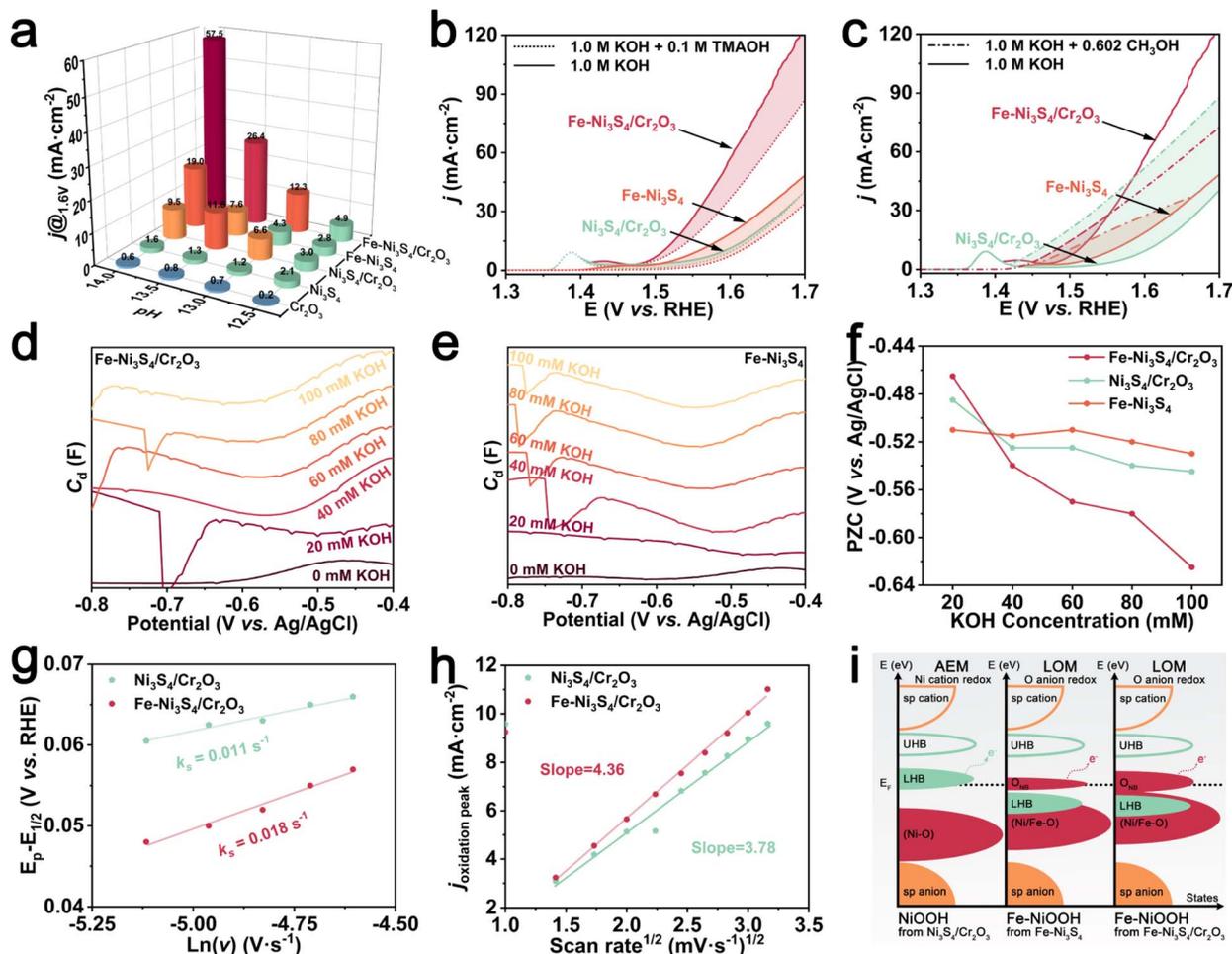
Fig. 5 (a) Current densities of Cr_2O_3, Ni_3S_4, Ni_3S_4/Cr_2O_3, Fe−Ni_3S_4, and Fe−Ni_3S_4/Cr_2O_3 at 1.6 V *vs.* RHE as a function of pH value. (b) Polarization curves for Ni_3S_4/Cr_2O_3, Fe−Ni_3S_4, and Fe−Ni_3S_4/Cr_2O_3 in 1.0 M KOH with and without TMAOH. (c) Polarization curves for Ni_3S_4/Cr_2O_3, Fe−Ni_3S_4, and Fe−Ni_3S_4/Cr_2O_3 in 1.0 M KOH with and without CH_3OH. Under different concentrations of KOH solutions, the differential capacitance (C_d) curves of (d) Fe−Ni_3S_4/Cr_2O_3, (e) Fe−Ni_3S_4. (f) PZC of Ni_3S_4/Cr_2O_3, Fe−Ni_3S_4, and Fe−Ni_3S_4/Cr_2O_3 in 20, 40, 80, and 100 mM KOH solutions. (g) K_s of Ni_3S_4/Cr_2O_3 and Fe−Ni_3S_4/Cr_2O_3. (h) Variations of anodic peak current densities for Ni_3S_4/Cr_2O_3 and Fe−Ni_3S_4/Cr_2O_3 electrodes as a function of the square root of scan rates. (i) Schematic energy bands relative to the Fermi level in consideration of Mott−Hubbard splitting.

typically used to assess whether specific adsorption occurs and to evaluate the adsorption capacity.[31] By gradually adding small amounts of KOH to the KCl solution, we obtained the PZC curve shown in Fig. 5f, which reflects the change in the PZC with varying amounts of KOH addition. As KOH concentration increased, the PZC values of Fe−Ni_3S_4/Cr_2O_3, Fe−Ni_3S_4 and Ni_3S_4/Cr_2O_3 became more negative, indicating specific OH^- adsorption on the catalyst's interphase (IPH) according to the Esin−Markov effect. Notably, Fe−Ni_3S_4/Cr_2O_3 showed a more pronounced shift in PZC with increasing KOH, suggesting that the Fe doping enhanced BIEF strengthens the catalyst's OH^- adsorption, enriching OH^- on the surface.

Further CV analysis at different scan rates (Fig. S16†) was performed to assess OH^- diffusion behavior on the electrode surface. The redox constant (K_s) was determined using the Laviron method, revealing that Fe−Ni_3S_4/Cr_2O_3 exhibited a higher K_s than Ni_3S_4/Cr_2O_3, indicating faster OH^- diffusion from the electrolyte to the electrode surface (Fig. 5g).[32,33]

Additionally, the diffusion coefficient of OH^- on Fe−Ni_3S_4/Cr_2O_3 was calculated to be 1.33 times that of Ni_3S_4/Cr_2O_3 using the Randles−Sevcik equation, supporting the conclusion that the Fe doping-enhanced BIEF accelerates OH^- diffusion kinetics (Fig. 5h).[34] These accelerated OH^- diffusion dynamics, combined with enhanced OH* deprotonation at the Fe−Ni_3S_4/Cr_2O_3 interface, optimize the OER activity of Fe−NiOOH *via* the LOM.

Using orbital hybridization theory, we explore how the Fe doping enhanced BIEF activates and optimizes the LOM of Fe−NiOOH, which is crucial for designing efficient OER catalysts (Fig. 5i).[6] The electronic states near the Fermi level are critical for determining the OER mechanism of a catalyst. The hybridization between the O 2p orbitals and Fe, Ni 3d orbitals, driven by differences in atomic electronegativity, results in the formation of bonding (M−O) and antibonding (M−O)* bands.[35] In the antibonding (M−O)* band, electrons are further localized by strong d−d Coulomb interactions, splitting into an empty

upper Hubbard band and a filled lower Hubbard band (LHB). The bonding M–O orbitals primarily exhibit oxygen-like characteristics, while the LHB in the antibonding orbitals exhibits metallic characteristics.[36] Oxygen and sulfur, being highly electronegative, cause significant charge transfer between metal and non-metal atoms.[27] Therefore, as a typical Mott–Hubbard insulator, the M–S or M–O electronic states near the Fermi level of Ni_3S_4/Cr_2O_3 and its reconstructed product NiOOH serve as the LHB. Thermodynamically, the metal acts as the primary redox center, with electron transfer occurring between the metal and the surface-adsorbed oxygen intermediates, following the AEM.

In Fe–NiOOH formed by the reconstruction of Fe–Ni_3S_4 or Fe–Ni_3S_4/Cr_2O_3, Fe doping optimizes the electronic states of Ni atoms, reduces the electronegativity difference between Ni and O atoms, lowers the energy required for charge transfer between atoms, and simultaneously enhances the d–d Coulomb interaction between electrons in the anti-bonding band. This allows the LHB to penetrate into the O 2p band, generating non-bonding oxygen states near the Fermi level.[7,37] This activates the redox behavior of oxygen atoms in the lattice, making electron transfer between lattice oxygen and oxygen intermediates possible during the OER process, thereby triggering the LOM. The coupling of lattice oxygen with adsorbed oxygen generates O_2^{2-}, avoiding the formation of the high-energy OOH* species in the AEM, breaking the scaling relationship limit, and accelerating the OER.[38,39] Furthermore, under the influence of the Fe doping enhanced BIEF at the heterogeneous interface, the surface of Fe–NiOOH formed from Fe–Ni_3S_4/Cr_2O_3 creates a localized high-efficiency electronic region. This further optimizes the hybridization between the metal and oxygen atomic orbitals, enhancing the covalency of metal–oxygen bonds and increasing the concentration of non-bonding oxygen states. The optimized metal d-band and oxygen p-band reduce energy consumption during the deprotonation process, thereby significantly enhancing OER activity.

4. Conclusion

In summary, we have significantly enhanced the OER activity of Fe–NiOOH, a reconstruction product of Fe–Ni_3S_4/Cr_2O_3, through doping modification and the construction of BIEF. In a 1 M KOH electrolyte, the catalyst exhibits an overpotential of 282 mV at a current density of 10 mA cm^{-2} and maintains stable performance for 100 h. Additionally, the catalyst demonstrates excellent resistance to oxidation and corrosion from Cl$^-$ ions in simulated seawater, preserving high OER activity. It also operates efficiently and stably for 40 h in a commercially scaled alkaline electrolyzer. Various characterization techniques have revealed the source of the exceptional catalytic performance. pH-dependence and TMAOH intermediate trapping experiments indicate that Fe doping optimized Fe–NiOOH metal–oxygen orbital hybridization activates the LOM. The activated lattice oxygen participates in the coupling of adsorbed oxygen, bypassing the formation of the high energy OOH* species typically generated in the traditional AEM. Band structure characterization and ICP testing indicate that the Fe doping

enhanced BIEF stabilizes the reconstruction of Fe–Ni_3S_4 with an electron-rich region at the heterogeneous interface, helping mitigate the decline in structural stability caused by ion leaching during the reaction process. Moreover, surface microenvironment characterization and methanol probe experiments demonstrate that the BIEF facilitates the OH$^-$ diffusion dynamics and HO* deprotonation process, which is the rate-limiting step in the LOM, further enhancing OER activity. This study highlights the effective structural regulation of the pre-catalyst reconstruction product using multiple modification strategies and establishes a structure–activity relationship between the pre-catalyst and OER performance.

Data availability

The data supporting this article have been included in the main text and the ESI.†

Author contributions

K. Wang, H. Xu and G. He conceived and designed this work. K. Wang and C. Ni carried out the synthesis and electrochemical measurements. All authors participated in the analysis of the data, discussed the results and revised the manuscript.

Conflicts of interest

There are no conflicts to declare.

Acknowledgements

References

1 L. Su, H. Wu, S. Zhang, C. Cui, S. Zhou and H. Pang, *Adv. Mater.*, 2025, **37**, 2414628.

2 Z. Qiu, X. Guo, S. Cao, M. Du, Q. Wang, Y. Pi and H. Pang, *Angew. Chem., Int. Ed.*, 2025, **64**, e202415216.

3 H. Yang, F. Li, S. Zhan, Y. Liu, W. Li, Q. Meng, A. Kravchenko, T. Liu, Y. Yang and Y. Fang, *Nat. Catal.*, 2022, **5**, 414–429.

4 T. Wu, Y. Sun, X. Ren, J. Wang, J. Song, Y. Pan, Y. Mu, J. Zhang, Q. Cheng and G. Xian, *Adv. Mater.*, 2023, **35**, 2207041.

5 J. Liang, K. Li, F. Shi, J. Li, J. n. Gu, Y. Xue, C. Bao, M. Guo, J. Jia and M. Fan, *Angew. Chem., Int. Ed.*, 2024, **63**, e202407870.

6 N. Zhang and Y. Chai, *Energy Environ. Sci.*, 2021, **14**, 4647–4671.

7 H. Wang, T. Zhai, Y. Wu, T. Zhou, B. Zhou, C. Shang and Z. Guo, *Adv. Sci.*, 2023, **10**, 2301706.

8 X. Wang, H. Zhong, S. Xi, W. S. V. Lee and J. Xue, *Adv. Mater.*, 2022, **34**, 2107956.

9 C.-X. Zhao, J.-N. Liu, C. Wang, J. Wang, L. Song, B.-Q. Li and Q. Zhang, *Energy Environ. Sci.*, 2022, **15**, 3257–3264.

10 Y. Hu, Y. Zheng, J. Jin, Y. Wang, Y. Peng, J. Yin, W. Shen, Y. Hou, L. Zhu and L. An, *Nat. Commun.*, 2023, **14**, 1949.

11 X. Liu, J. Meng, J. Zhu, M. Huang, B. Wen, R. Guo and L. Mai, *Adv. Mater.*, 2021, **33**, 2007344.

12 H. Xu, L. Yang, Y. Liu, L. Jin, K. Wang, G. He and H. Chen, *Fuel*, 2024, **377**, 132796.

13 K. Wang, H. Xu, H. Xing, L. Jin, X. Qian, G. He and H. Chen, *Chem. Eng. J.*, 2024, **500**, 157316.

14 H. Ding, H. Liu, W. Chu, C. Wu and Y. Xie, *Chem. Rev.*, 2021, **121**, 13174–13212.

15 M. J. Craig, G. Coulter, E. Dolan, J. Soriano-López, E. Mates-Torres, W. Schmitt and M. García-Melchor, *Nat. Commun.*, 2019, **10**, 4993.

16 Y. Lyu, J. Zheng, Z. Xiao, S. Zhao, S. P. Jiang and S. Wang, *Small*, 2020, **16**, 1906867.

17 H. Xu, L. Yang, L. Jin, Y. Liu, K. Wang, J. Chen, G. He and H. Chen, *J. Colloid Interface Sci.*, 2025, **677**, 158–166.

18 S. Zhang, C. Tan, R. Yan, X. Zou, F. L. Hu, Y. Mi, C. Yan and S. Zhao, *Angew. Chem., Int. Ed.*, 2023, **135**, e202302795.

19 W. Li, L. Zhao, X. Jiang, Z. Chen, Y. Zhang and S. Wang, *Adv. Funct. Mater.*, 2022, **32**, 2207727.

20 N. Wang, P. Ou, S. F. Hung, J. E. Huang, A. Ozden, J. Abed, I. Grigioni, C. Chen, R. K. Miao and Y. Yan, *Adv. Mater.*, 2023, **35**, 2210057.

21 J. Guo, Y. Zheng, Z. Hu, C. Zheng, J. Mao, K. Du, M. Jaroniec, S.-Z. Qiao and T. Ling, *Nat. Energy*, 2023, **8**, 264–272.

22 P. Zhao, S. Fu, Y. Luo, C. Peng, L. Cheng and Z. Jiao, *Small*, 2023, **19**, 2305241.

23 Y. Lu, C. L. Dong, Y. C. Huang, Y. Zou, Z. Liu, Y. Liu, Y. Li, N. He, J. Shi and S. Wang, *Angew. Chem., Int. Ed.*, 2020, **59**, 19215–19221.

24 H. Liu, W. Shen, H. Jin, J. Xu, P. Xi, J. Dong, Y. Zheng and S. Z. Qiao, *Angew. Chem., Int. Ed.*, 2023, **62**, e202311674.

25 H. Lei, L. Ma, Q. Wan, S. Tan, B. Yang, Z. Wang, W. Mai and H. J. Fan, *Adv. Energy Mater.*, 2022, **12**, 2202522.

26 A. Grimaud, O. Diaz-Morales, B. Han, W. T. Hong, Y.-L. Lee, L. Giordano, K. A. Stoerzinger, M. T. Koper and Y. Shao-Horn, *Nat. Chem.*, 2017, **9**, 457–465.

27 X. Li, C. Deng, Y. Kong, Q. Huo, L. Mi, J. Sun, J. Cao, J. Shao, X. Chen and W. Zhou, *Angew. Chem., Int. Ed.*, 2023, **62**, e202309732.

28 C. Yang, O. Fontaine, J. M. Tarascon and A. Grimaud, *Angew. Chem., Int. Ed.*, 2017, **129**, 8778–8782.

29 H. B. Tao, Y. Xu, X. Huang, J. Chen, L. Pei, J. Zhang, J. G. Chen and B. Liu, *Joule*, 2019, **3**, 1498–1509.

30 B. Huang, J. Yan, Z. Li, L. Chen and J. Shi, *Angew. Chem., Int. Ed.*, 2024, e202409419.

31 C. Liu, G. Zhang, W. Zhang, Z. Gu and G. Zhu, *Proc. Natl. Acad. Sci. U.S.A.*, 2023, **120**, e2209979120.

32 E. Laviron, *J. Electroanal. Chem. Interfacial Electrochem.*, 1979, **100**, 263–270.

33 Z. Xiao, Y.-C. Huang, C.-L. Dong, C. Xie, Z. Liu, S. Du, W. Chen, D. Yan, L. Tao and Z. Shu, *J. Am. Chem. Soc.*, 2020, **142**, 12087–12095.

34 T. Brezesinski, J. Wang, J. Polleux, B. Dunn and S. H. Tolbert, *J. Am. Chem. Soc.*, 2009, **131**, 1802–1809.

35 Z. Wang, W. A. Goddard III and H. Xiao, *Nat. Commun.*, 2023, **14**, 4228.

36 H. Wu, Q. Huang, Y. Shi, J. Chang and S. Lu, *Nano Res.*, 2023, **16**, 9142–9157.

37 S. Xin, Y. Tang, B. Jia, Z. Zhang, C. Li, R. Bao, C. Li, J. Yi, J. Wang and T. Ma, *Adv. Funct. Mater.*, 2023, **33**, 2305243.

38 H. Jin, X. Liu, P. An, C. Tang, H. Yu, Q. Zhang, H.-J. Peng, L. Gu, Y. Zheng and T. Song, *Nat. Commun.*, 2023, **14**, 354.

39 R. Chen, Z. Wang, S. Chen, W. Wu, Y. Zhu, J. Zhong and N. Cheng, *ACS Energy Lett.*, 2023, **8**, 3504–3511.